Co atom moves from the fcc site to the hcp site for three molecular lengths. As the Cu chain increases, so does the energy difference between fcc and hcp sites and the energy barrier dividing them (Fig. 4B). These trends correspond to a stabilization of the linear configuration of the molecule and explain the experimental observation of increased stability of the fcc site as n increases (Figs. 3B and 4A). The motion of the Co atom becomes progressively hindered as the Cu chain length increases, because more atoms in the Cu chain must bend away from their energetically favored fcc positions, as is illustrated in Fig. 4C, where the resulting lateral shifts of the Cu chain atoms from their ideal positions are plotted for different chain lengths.

Because the smallest atomic-scale switch will likely involve modulating the electrical conductivity through the control of a single atom, the extension of studies such as this to semiconductor and insulating thin films could point the way to new classes of atomic-scale electronic and magnetic devices.

References and Notes

1. D. M. Eigler, E. K. Schweizer, *Nature* **344**, 524 (1990).
2. J. A. Stroscio, D. M. Eigler, *Science* **254**, 1319 (1991).
3. L. Bartels, G. Meyer, K.-H. Rieder, *Phys. Rev. Lett.* **79**, 697 (1997).
4. D. M. Eigler, C. P. Lutz, W. E. Rudge, *Nature* **352**, 600 (1991).
5. B. C. Stipe, M. A. Rezaei, W. Ho, *Science* **279**, 1907 (1998).
6. T. Komeda, Y. Kim, M. Kawai, B. N. J. Persson, H. Ueba, *Science* **295**, 2055 (2002).
7. A. J. Heinrich, C. P. Lutz, J. A. Gupta, D. M. Eigler, *Science* **298**, 1381 (2002); published online 24 October 2002 (10.1126/science.1076768).
8. W. Ho, *J. Chem. Phys.* **117**, 11033 (2002).
9. J. I. Pascual *et al.*, *Nature* **423**, 525 (2003).
10. J. A. Stroscio, R. J. Celotta, *Science* **306**, 242 (2004); published online 9 September 2004 (10.1126/science.1102370).
11. M. Lastapis *et al.*, *Science* **308**, 1000 (2005).
12. K.-Y. Kwon *et al.*, *Phys. Rev. Lett.* **95**, 166101 (2005).
13. Measurements were made in a cryogenic ultrahigh-vacuum STM instrument of our own design. We deposited Co and Cu atoms onto a Cu(111) surface, which was initially cleaned by ion sputtering and annealing. Co and Cu atoms can be chemically distinguished on the Cu(111) surface on the basis of STM spectroscopy measurements of the Co Kondo resonance. STM measurements were made by using Ir probe tips and a substrate temperature of 4.3 K.
14. B. N. J. Persson, A. Baratoff, *Phys. Rev. Lett.* **59**, 339 (1987).
15. J. W. Gadzuk, *Phys. Rev. B* **44**, 13466 (1991).
16. G. P. Salam, M. Persson, R. E. Palmer, *Phys. Rev. B* **49**, 10655 (1994).
17. S. Gao, M. Persson, B. I. Lundqvist, *Phys. Rev. B* **55**, 4825 (1997).
18. S. Fölsch, P. Hyldgaard, R. Koch, K. H. Ploog, *Phys. Rev. Lett.* **92**, 056803 (2004).

19. We thank S. Blankenship for technical assistance and are grateful for several fruitful discussions with J. W. Gadzuk, D. Penn, and M. Stiles. This work was supported in part by the Office of Naval Research.

Supporting Online Material

www.sciencemag.org/cgi/content/full/313/5789/948/DC1
Fig. S1

10 May 2006; accepted 11 July 2006
10.1126/science.1129788

Controlling the Electronic Structure of Bilayer Graphene

Taisuke Ohta,[1,2]* Aaron Bostwick,[1]* Thomas Seyller,[3] Karsten Horn,[2] Eli Rotenberg[1]†

We describe the synthesis of bilayer graphene thin films deposited on insulating silicon carbide and report the characterization of their electronic band structure using angle-resolved photoemission. By selectively adjusting the carrier concentration in each layer, changes in the Coulomb potential led to control of the gap between valence and conduction bands. This control over the band structure suggests the potential application of bilayer graphene to switching functions in atomic-scale electronic devices.

Carbon-based materials such as carbon nanotubes (CNTs), graphite intercalation compounds, fullerenes, and ultrathin graphite films exhibit many exotic phenomena such as superconductivity (*1*–*3*) and an anomalous quantum Hall effect (*4*–*6*). These findings have caused renewed interest in the electronic structure of ultrathin layers of graphite, such as graphene: a single hexagonal carbon layer that is the building block for these materials. There is a strong motivation to incorporate graphene multilayers into atomic-scale devices, spurred on by rapid progress in their fabrication and manipulation.

We studied the valence band (VB) structure of a bilayer of graphene and demonstrated that through selective control of the carrier concentration in the graphene layers, one can easily tune the band structure near the Dirac crossing. Similar control can be achieved in principle by varying the electric field across the bilayer film in an atomic-scale switching device.

The electronic states of graphene can be well described within basic calculational schemes (*7*–*9*). Graphene is a flat layer of carbon atoms arranged in a hexagonal lattice with two carbon atoms per unit cell. Of the four valence states, three sp^2 orbitals form a σ state with three neighboring carbon atoms, and one p orbital develops into delocalized π and π* states that form the highest occupied VB and the lowest unoccupied conduction band (CB). The π and π* states of graphene are degenerate at the corner (K point) of the hexagonal Brillouin zone (BZ) (Fig. 1A). This degeneracy occurs at the so-called Dirac crossing energy E_D, which at the normal half-filling condition coincides with the Fermi level (E_F), resulting in a pointlike metallic Fermi surface (Fig. 2E).

Strictly speaking, undoped graphene is a semimetal because although there is a state crossing at $E_D = E_F$, the density of states there is zero and conduction is possible only with thermally excited electrons at finite temperature. In applying an effective mass description for the VB and CB (*7*), one arrives at a formal equivalence between the resulting differential equation and the Dirac equation, hence charge carriers in the vicinity of E_F may be termed "Dirac fermions" (with the crossing point at K being named the Dirac point). Moreover, the particular band structure at the BZ boundary (that is, a linear dispersion) leads to an effective mass $m^* = 0$ at the point where the VB and CB meet. The peculiar band structure in ultrathin graphite layers results in a number of unusual electronic transport properties, such as an anomalous quantum Hall effect (*4*–*6*, *10*).

The graphene band structure is sensitive to the lattice symmetry. If the hexagonal layer structure is composed of nonequivalent elements, such as in boron nitride, the lateral, in-plane symmetry is broken, resulting in the formation of a large gap between π and π* states (*11*). The symmetry can also be broken with respect to the c axis by stacking two graphene layers in Bernal stacking (the stacking fashion of graphite) as suggested by McCann and Fal'ko (*12*) (Fig. 1B). Because the unit cell of a bilayer contains four atoms, its band structure acquires two additional bands, π and π* states, in each valley split by interlayer (A-B) coupling, and two lower energy bands. If the individual graphene layers in a bilayer are rendered inequivalent (Fig. 1C), then an energy gap between low-energy bands forms at the former Dirac crossing point (*12*). Provided that the charge state is such that E_F lies within the gap, a semimetal-to-insulator transition occurs. If this symmetry breaking could be controlled externally, the electronic conductivity would change through this transition, suggesting that a switch with a thickness of two atomic layers could be constructed.

To see whether this gedanken experiment can be realized, we synthesized bilayer graphene

[1]Advanced Light Source, Lawrence Berkeley National Laboratory, One Cyclotron Road, Berkeley, CA 94720, USA. [2]Department of Molecular Physics, Fritz-Haber-Institut, der Max-Planck-Gesellschaft, Faradayweg 4-6, D-14195 Berlin, Germany. [3]Institut für Physik der Kondensierten Materie, Universität Erlangen-Nürnberg, Erwin-Rommel-Strasse 1, D-91058 Erlangen, Germany.

*These authors contributed equally to this work.
†To whom correspondence should be addressed.

films on a silicon carbide (SiC) substrate [6H polytype with (0001) orientation], following the recipe in (*13*), and measured their electronic properties using angle-resolved photoemission spectroscopy (ARPES) (*14*). As initially grown, our films had a slight *n*-type doping, acquired by depletion of the substrate's dopant carriers. Because we measured at low temperature, the dopant electrons in the SiC were frozen out and the substrate was a nearly perfect insulator, whereas the excess carriers left in the film, having been separated from their dopant atoms, had high mobility. Because the SiC states are well separated from both E_F and E_D [the SiC VB lies ~2.6 eV below E_F and the CB ~0.4 eV above E_F (*15*)], we can regard the bilayer graphene states as practically decoupled from the substrate and therefore as representing a true two-dimensional semimetal.

These films can sustain high current densities. At a temperature of 30 K, which is cold enough to preclude any conduction through the substrate, we can pass 400 mA through a macroscopic sample (5 by 15 mm), corresponding to a current of ~1 nA (10^{10} to ~10^{11} electrons/s) per graphene C atom, which is the same order of magnitude reported for single-walled CNTs (*16*) and graphene multilayers (*10*).

The symmetry of the bilayers is broken by the dipole field created between the depletion layer of the SiC and the accumulation of charge on the graphene layer next to the interface, rendering the two graphene layers inequivalent with respect to charge and electrostatic potential in the as-prepared films. We can induce further *n*-type doping by the deposition of potassium atoms onto the vacuum side, which donate their lone valence electrons to the surface layer, forming another dipole (*17*, *18*). These surface and interface dipole fields together act as the symmetry-breaking factor, which controls the presence or absence of the gap at the crossing energy E_D (Fig. 1, B and C). The net dipole field between the two graphene layers results from the short screening length (~4 Å) along the *c* axis (*7*), which is comparable to the layer thickness (~3.4 Å). A similar charge localization has been observed at the surface of graphite and graphene multilayers in an externally applied field (*19*, *20*).

Figure 2, A to C, shows the binding energy–momentum dispersion relation of π, π*, and σ states along high-symmetry directions measured by ARPES. The ~0.4-eV splitting of the π state (as in Fig. 1B) confirms that the sample is composed predominantly of two graphene layers (*14*). In Fig. 2, A and B, the crossing point E_D can be clearly observed because this bilayer is *n*-type–doped through carrier depletion from the SiC substrate. In the constant-energy contours in the momentum space of π and π* states near E_F (Fig. 2, D to F), we can clearly see the electron and hole pockets above and below E_D, respectively. Besides the primary bilayer graphene states, we can identify six weak replicas of the π and π* states surrounding the primary states, especially in Fig. 2F. Low-energy electron diffraction shows that graphene layers grown on the SiC substrate display a nearly commensurate superstructure with relative lattice constant ($6\sqrt{3} \times 6\sqrt{3}$) rotated 30° with respect to the substrate because of the difference between the graphene lattice constant of ~2.46 Å and that of SiC, 3.07 Å (*21*). The replicas of the π and π* states are presumably brought about by scattering off of this superstructure in a fashion similar to those in other nearly incommensurate systems (*22*, *23*).

The effects of doping the bilayers are shown in Fig. 3, which compares the as-prepared film (Fig. 3A) to two coverages of potassium. Our samples consisted predominantly of bilayer graphene, but depending on preparation conditions, we found minority regions of single- or triple-layer graphene within our probe area; the contribution of these minority domains has been subtracted from the data in Fig. 3. Beside the more or less rigid shift of the π and π* states toward higher binding energy because of an increased carrier concentration, the upper unoccupied π* state drops below E_F at n = 0.0125 electron per unit cell (Fig. 3B) and continues dropping down with higher potassium coverage. The electron carrier densities of each stage are determined from the relative sizes of the Fermi surfaces with respect to the surface BZ of graphite.

Plotted next to the intensity maps are calculated tight-binding bands (solid lines) (*12*), where the low-lying electronic states near the K point of the BZ are described by the solution of a simple 4 × 4 Hamiltonian as

$$\varepsilon_\alpha(k) = \pm\left[\frac{\gamma_1^2}{2} + \frac{U^2}{4} + \left(v^2 + \frac{v_3^2}{2}\right)k^2 + (-1)^\alpha\sqrt{\Gamma}\right]^{1/2}$$

where the band index α = 1,2 and

$$\Gamma = \frac{1}{4}(\gamma_1^2 - v_3^2k^2)^2 + v^2k^3(\gamma_1^2 + U^2 + v_3^2k^2) + 2\gamma_1 v_3 v^2 k^3 \cos 3\phi$$

and $v_3 = \sqrt{3}\, a\gamma_3/2\hbar$.

Here k is the momentum in Å^{-1}, ϕ is the azimuthal angle, v is the band velocity (m/s × $\hbar$ ×

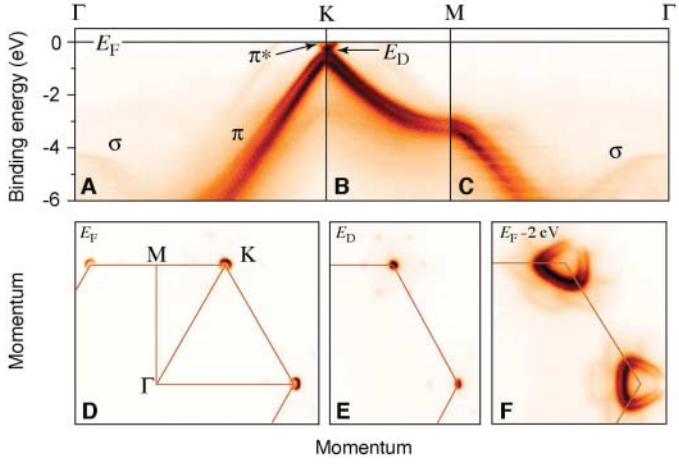

Fig. 2. Energy-momentum dispersion relation of π, π*, and σ states of bilayer graphene. (**A** to **C**) Energy-momentum dispersion along high-symmetry directions. (**D** to **F**) Constant energy contours at E_F, E_F –0.4 eV = E_D, and E_F –2 eV. The high-symmetry points, directions, and BZ zone boundaries are indicated in (D).

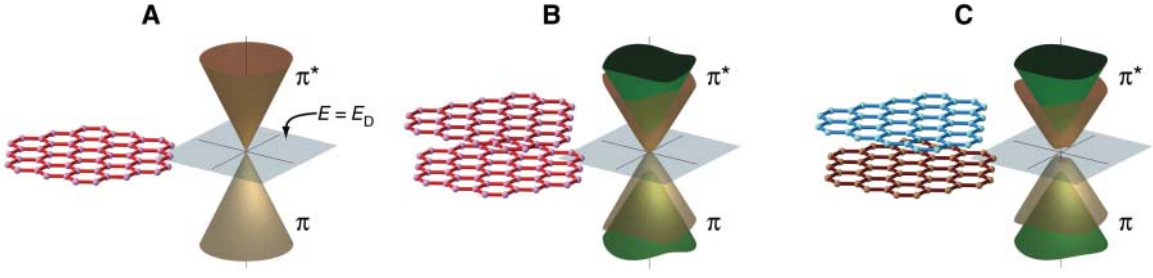

Fig. 1. Electronic structure of a single (**A**), symmetric double layer (**B**), and asymmetric double layer (**C**) of graphene. The energy bands depend only on in-plane momentum because the electrons are restricted to motion in a two-dimensional plane. The Dirac crossing points are at energy E_D.

10^{10}), U is the difference in the onsite Coulomb potentials of the two layers, γ_1 (eV) and γ_3 (eV) are out-of-plane nearest-neighbor and next–nearest-neighbor interaction parameters, and a (Å) is the graphite lattice constant (*24*, *25*). These parameters are adjusted to reproduce the measured band structures over a large energy range (*14*). U is chosen to match the gap at the K point.

The most important feature in Fig. 3 is the variation in the apparent gap at the K point: first open in Fig. 3A, then closed in Fig. 3B, and finally open again in Fig. 3C. This gap variation is reproduced by our tight-binding calculation and is attributed to the variation in the relative potentials of the two layers as discussed above. Away from the K point, the gap is generally smaller than the prediction because the cusps extending into the gap between the π and π* bands are much sharper than in the model. As a result, the gap for the uncovered film (Fig. 3A) is not clearly resolved, although a shift of the bands is readily apparent from the flattening of the π* band edge and the lack of spectral weight at E_D. Sufficient asymmetry was developed for higher doping that the gap is unambiguously open in Fig. 3C.

The measured π* state of bilayer graphene (Fig. 3C) does not agree with the tight-binding band, particularly around 200 meV below E_F, where a slight kink is observed in the bands. This is presumably due to electron mass renormalization by electron-phonon coupling.

In order to systematically follow the evolution of the gap between π and π* states, photoemission spectra at the K point (the center cut of the bands in Fig. 3) as a function of doping are shown in Fig. 4A. The blue markers are the positions of the tight-binding π and π* bands. The data and calculated energies of the π and π* states clearly display the closing and reopening of the gap. The yellow line is the energy difference $E_F - E_D$, which increases by about 0.32 eV with respect to the as-grown sample, reflecting the overall doping level of the film.

The variation of carrier concentration has a marked influence on the band structure as derived from a comparison of the experimental results with the tight-binding calculation (Fig. 4). The Coulomb potential difference U displays a sign change at the electron concentration where the gap closes. It is expected that U increases with an increase of the charge difference in either graphene layer, induced by the fields at the respective interfaces. We have estimated the potential of each graphene layer from Poisson's equation, based on the Schottky barrier height of 0.4 eV (*15*), assuming infinitely thick graphene multilayers, and find that for the as-prepared sample, the potential difference between the first and second layers shows reasonable agreement with the Coulomb potential difference U estimated from the size of the gap evaluated in the tight-binding model. The resulting electric field in the graphene layers is similar in magnitude to that induced in a device structure (*26*). Moreover, a monotonic increase is seen in γ_1, which measures the interlayer interaction as a function of electron concentration in both layers. This suggests that at higher electron density, the overlap between π orbitals of adjacent graphene layers increases. This may be due to the smaller interlayer distance caused by a shorter screening length.

Our results demonstrate that by controlling the carrier density in a bilayer of graphene, the occupation of electronic states near E_F and the magnitude of the gap between the VB and CB can be manipulated. We have chosen potassium doping as a means of achieving this, but the switching functionality may be readily induced by an electric field across the bilayer in a device structure, in such a way that the potentials on either layer have opposite sign (*10*). The deposition of alkali atoms on epitaxially grown multilayer graphene films thus provides, beyond an opportunity to obtain their wave vector–resolved electronic structure as reported here, a path to studying their physical properties in a devicelike context.

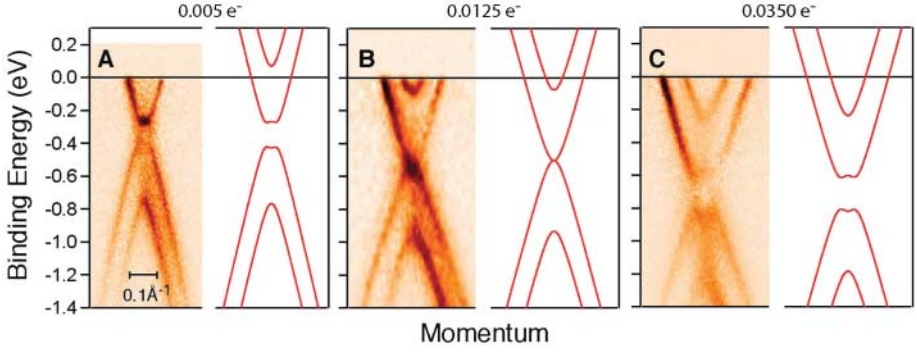

Fig. 3. Evolution of gap closing and reopening by changing the doping level by potassium adsorption. Experimental and theoretical bands (solid lines) (**A**) for an as-prepared graphene bilayer and (**B** and **C**) with progressive adsorption of potassium are shown. The number of doping electrons per unit cell, estimated from the relative size of the Fermi surface, is indicated at the top of each panel.

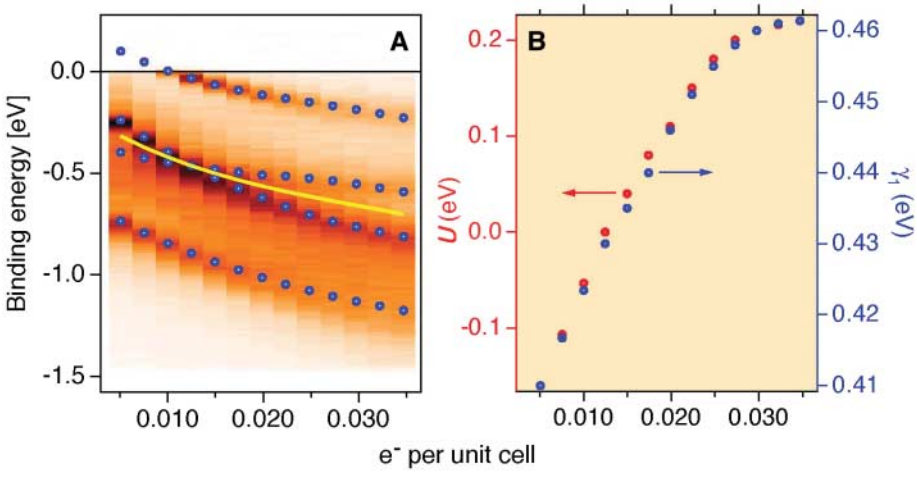

Fig. 4. Variation of states at the K point with increasing potassium coverage. (**A**) The image map shows the energy distribution curve at K as a function of potassium coverage. The blue markers are the fitted positions of the tight-binding π and π* bands, and the yellow line indicates E_D. The closing and reopening of the gap between π and π* states are clearly shown. (**B**) The influence of doping concentration on the band parameters U and γ_1.

References and Notes

1. Z. K. Tang *et al.*, *Science* **292**, 2462 (2001).
2. N. B. Hannay *et al.*, *Phys. Rev. Lett.* **14**, 225 (1965).
3. T. E. Weller, M. Ellerby, S. S. Saxena, R. P. Smith, N. T. Skipper, *Nat. Phys.* **1**, 39 (2005).
4. K. S. Novoselov *et al.*, *Nature* **438**, 197 (2005).
5. Y. Zhang, Y.-W. Tan, H. L. Stormer, P. Kim, *Nature* **438**, 201 (2005).
6. K. S. Novoselov *et al.*, *Nat. Phys.* **2**, 177 (2006).
7. D. P. DiVincenzo, E. J. Mele, *Phys. Rev. B* **29**, 1685 (1984).
8. P. R. Wallace, *Phys. Rev.* **71**, 622 (1947).
9. S. Reich, J. Maultzsch, C. Thomsen, P. Ordejón, *Phys. Rev. B* **66**, 035412 (2002).
10. K. S. Novoselov *et al.*, *Science* **306**, 666 (2004).
11. X. Blase, A. Rubio, S. G. Louie, M. L. Cohen, *Phys. Rev. B* **51**, 6868 (1995).
12. E. McCann, V. I. Fal'ko, *Phys. Rev. Lett.* **96**, 086805 (2006).
13. I. Forbeaux, J.-M. Themlin, J.-M. Debever, *Phys. Rev. B* **58**, 16396 (1998).
14. Information on materials and methods is available as supporting material on *Science* Online.
15. Th. Seyller, K.V. Emtsev, F. Speck, K.-Y. Gao, L. Ley, *Appl. Phys. Lett.* **88**, 242103 (2006).

16. Z. Yao, C. L. Kane, C. Dekker, *Phys. Rev. Lett.* **84**, 2941 (2000).
17. At 30 K, the mobility of the potassium atoms is substantially reduced as compared to that at 90 K, where the condensed phase of potassium atoms is found (*18*). It is thus reasonable to assume that the potassium atoms mainly adsorb onto and interact with the surface of the graphene layer in the low-temperature deposition we used (around 30 K).
18. K. M. Hock, R. E. Palmer, *Surf. Sci.* **284**, 349 (1993).
19. Y. Zhang, J. P. Small, W. V. Pontius, P. Kim, *Appl. Phys. Lett.* **86**, 073104 (2005).
20. K. S. Novoselov, F. Schedin, D. Jiang, A. A. Firsov, A. K. Geim, *Phys. Rev. B* **72**, 201401 (2005).
21. I. Forbeaux, J.-M. Themlin, J.-M. Debever, *Phys. Rev. B* **58**, 16396 (1998).
22. J. N. Crain, K. N. Altmann, C. Bromberger, F. J. Himpsel, *Phys. Rev. B* **66**, 205302 (2002).
23. Eli Rotenberg *et al.*, *Phys. Rev. Lett.* **91**, 246404 (2003).
24. J. C. Slonczewski, P. R. Weiss, *Phys. Rev.* **109**, 272 (1958).
25. J. W. McClure, *Phys. Rev.* **108**, 612 (1957).
26. S. V. Morozov *et al.*, *Phys. Rev. B* **72**, 201401 (2005).
27. This work and the Advanced Light Source were supported by the U.S. Department of Energy, Office of Basic Sciences. K.H. and T.O. were supported by the Max Planck Society and the European Science Foundation under the EUROCORES SONS program.

Supporting Online Material
www.sciencemag.org/cgi/content/full/313/5789/952/DC1
Materials and Methods
Figs. S1 to S3
References

31 May 2006; accepted 12 July 2006
10.1126/science.1130681

Two-Dimensional Nematic Colloidal Crystals Self-Assembled by Topological Defects

Igor Muševič,[1,2]* Miha Škarabot,[1] Uroš Tkalec,[1] Miha Ravnik,[2] Slobodan Žumer[2,1]

The ability to generate regular spatial arrangements of particles is an important technological and fundamental aspect of colloidal science. We showed that colloidal particles confined to a few-micrometer-thick layer of a nematic liquid crystal form two-dimensional crystal structures that are bound by topological defects. Two basic crystalline structures were observed, depending on the ordering of the liquid crystal around the particle. Colloids inducing quadrupolar order crystallize into weakly bound two-dimensional ordered structure, where the particle interaction is mediated by the sharing of localized topological defects. Colloids inducing dipolar order are strongly bound into antiferroelectric-like two-dimensional crystallites of dipolar colloidal chains. Self-assembly by topological defects could be applied to other systems with similar symmetry.

Dispersions of colloids or liquid droplets in a nematic liquid crystal show a diversity of self-assembled structures, such as linear chains (*1*, *2*), anisotropic clusters (*3*), two-dimensional (2D) hexagonal lattices at interfaces (*4*, *5*), arrays of defects (*6*), particle-stabilized gels (*7*), and cellular soft-solid structures (*8*). The ability of liquid crystals to spontaneously arrange foreign particles into regular geometric patterns is therefore highly interesting for developing new approaches to building artificial colloidal structures, such as 3D photonic band-gap devices (*9*). Current approaches to fabrication rely on the controlled sedimentation of colloids from solutions (*10*), growth on patterned and prefabricated templates on surfaces (*11*), external-field–assisted manipulation (*12*), and precision lithography combined with mechanical micromanipulation (*13*).

In isotropic solvents, the spatial aggregation of colloids is controlled by a fine balance between the attractive dispersion forces and the Coulomb, steric, and other repulsive forces. The nature of colloidal interactions in nematic liquid crystals is quite different. Nematic liquid crystals are orientationally ordered complex fluids, in which rodlike molecules are spontaneously and collectively aligned into a certain direction, called the director. Because of their anisotropy, the orientation of nematic liquid crystals can be manipulated by external electric or magnetic fields, or even by anisotropic surfaces, which is an important issue in liquid crystal display technology. When foreign particles are introduced into the nematic liquid crystal, the orientation of nematic molecules is locally disturbed because of their interaction with the surfaces of the inclusions. The disturbance spreads on a long (micrometer) scale and can be considered as an elastic deformation of the nematic liquid crystal. Because the elastic energy of deformation depends on the separation between inclusions, structural forces between inclusions are generated. The structural forces in liquid crystals are long-range (on the order of micrometers) and spatially highly anisotropic, thus reflecting the nature of the order in liquid crystals (*14*–*17*).

In our experiments, a dispersion of micrometer-sized silica spheres in the nematic liquid crystal pentylcyanobiphenyl (5CB) was introduced into a rubbed thin glass cell with thickness varying along the direction of rubbing from

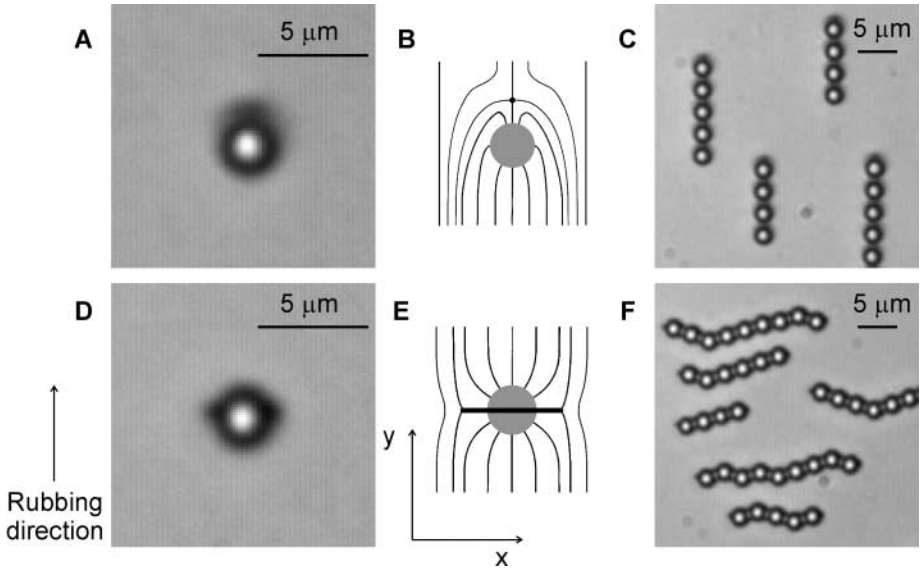

Fig. 1. Dipolar and quadrupolar colloids in a thin layer of a nematic liquid crystal. (**A**) Micrograph of a $d = 2.32$ μm silica sphere in an $h = 5$ μm layer of 5CB with a hyperbolic hedgehog defect (black spot on top). (**B**) The nematic order around the colloid has the symmetry of an electric dipole. (**C**) Dipoles spontaneously form dipolar (ferroelectric) chains along the rubbing direction. (**D**) The same type of colloid in a thin ($h = 2.5$ μm) 5CB layer. The two black spots on the right and left side of the colloid represent the Saturn ring. (**E**) The nematic order has in this case the symmetry of an electric quadrupole. (**F**) Quadrupoles spontaneously form kinked chains perpendicular to the direction of rubbing.

[1]J. Stefan Institute, Jamova 39, 1000 Ljubljana, Slovenia. [2]Faculty of Mathematics and Physics, University of Ljubljana, Jadranska 19, 1000 Ljubljana, Slovenia.

*To whom correspondence should be addressed. E-mail: igor.musevic@ijs.si